Rare Metal Materials and Engineering
Volume 55, Issue 11, November 2026
Available online at www.rmme.ac.cn

Science Press

Cite this article as: Xu Lianbo, Li Xinlei, Gui Yongliang, et al. Influence of Mo Content on Microstructure, Wear Resistance, and Corrosion Behavior of $NbTiZrMo_x$ Refractory High-Entropy Alloys[J]. Rare Metal Materials and Engineering, 2026, 55(11): 2765-2775. DOI: https://doi.org/10.12442/j.issn.1002-185X.20250655.

ARTICLE

Influence of Mo Content on Microstructure, Wear Resistance, and Corrosion Behavior of $NbTiZrMo_x$ Refractory High-Entropy Alloys

Xu Lianbo[1], Li Xinlei[1], Gui Yongliang[1], Song Chunyan[1], Long Haiyang[2], Han Shangda[1], Yang Yusheng[1], Wu Qiming[1]

[1] College of Metallurgy and Energy, North China University of Science and Technology, Tangshan 063210, China; [2] College of Mechanical Engineering, North China University of Science and Technology, Tangshan 063210, China

Abstract: $NbTiZrMo_x$ alloys were prepared by vacuum arc furnace with high-purity powder mixtures of Nb, Ti, Zr, and Mo as raw materials. The role of element Mo in $NbTiZrMo_x$ alloys and the effect of different Mo content on microstructure, microhardness, wear resistance, and corrosion resistance of $NbTiZrMo_x$ alloys were investigated. Results show that these alloys display a typical dendritic morphology with a single-phase body-centered cubic crystal structure. The microhardness and wear resistance of $NbTiZrMo_x$ alloys are significantly improved with the increase in Mo content, which is attributed to solid-solution strengthening and fine-grain strengthening. With the increase in Mo content, the dominant wear mechanism of the alloy transforms from adhesive wear accompanied by abrasive and oxidative wear to oxidative wear with slight adhesive wear. Electrochemical corrosion tests conducted in a 3.5wt% NaCl solution reveal that the corrosion resistance of $NbTiZrMo_x$ alloys exhibits a trend of initial enhancement followed by deterioration as Mo content rises. The alloy containing 14.29at% Mo achieves the optimal corrosion resistance, demonstrating that an appropriate addition of Mo facilitates the formation of a stable passive film and thereby markedly improves the corrosion resistance of the alloy.

Key words: $NbTiZrMo_x$ refractory high-entropy alloys; microstructure; wear resistance; corrosion resistance

1 Introduction

Failure of critical components in marine equipment (e. g., flange components in seawater purification devices) from corrosion by high-salinity seawater or abrasion by marine sand particles is non-negligible[1–3]. Therefore, the development of novel high-performance materials with both excellent wear resistance and corrosion resistance to resist mechanical abrasion and seawater corrosion damage is crucial to extend the service life and enhance the operational safety of critical marine components.

In recent years, refractory high-entropy alloys (RHEAs) have provided an effective approach to address this challenge. By virtue of their unique intrinsic effects, including the high-entropy effect, lattice distortion effect, sluggish diffusion effect, and "cocktail" effect[4–6], RHEAs have exhibited excellent characteristics surpassing those of traditional alloys, including outstanding wear resistance, corrosion resistance, biocompatibility, and high strength[7–11]. Research on RHEAs began with the NbMoTaW and HfNbTaTiZr alloys reported by Senkov et al[12], however, these alloys cannot possess excellent plasticity and strength simultaneously. To address these restrictions, numerous studies in recent years have developed a range of RHEAs, such as $Al_{53}Hf_{10}Nb_{8.5}Ta_8Ti_{7.5}Zr_{13}$ [13], $Al_{0.5}Nb_{1.5}TiV_2Zr_{0.5}$ [14], and ZrNbTaTi[15]. These newly designed alloys all demonstrate excellent room-temperature tensile ductility (>10%) in the as-cast state. Among them, the $Zr_{45}Ti_{15}Nb_{20}Ta_{20}$ alloy possesses a yield strength of approximately 1087 MPa and a fracture elongation of 11.8%. Hu et al[16] constructed a phase diagram for single-phase body-centered

Received date: December 30, 2025
Foundation item: Science and Technology Program of Hebei (246Z1019G)
Corresponding author: Gui Yongliang, Ph. D., Professor, College of Metallurgy and Energy, North China University of Science and Technology, Tangshan 063210, P. R. China, E-mail: gyl@ncst.edu.cn

cubic (bcc) RHEAs comprising 182 826 compositions based on nine elements: Ti, V, Cr, Zr, Nb, Mo, Hf, Ta, and W. This work revealed the immense potential of RHEAs for ultra-high-strength engineering applications while also highlighting their common challenges in plasticity (only 6.6% of compositions with valence electron concentration<4.5) and lightweighting (only 7.6% of compositions with density<8 g/cm^3). Among various RHEA systems, considerable attention has been devoted to NbTiZr-based alloys in the materials research community, as they are endowed with low density, high specific strength, excellent wear and corrosion resistance, and superior room-temperature plasticity[17–19]. A Ti-25Nb-10Zr alloy has been fabricated by the cold crucible levitation melting technique, whose plasticity (48.94%) is significantly higher than that of NbMoTaW (merely 10%) and the as-cast TiVNbTa (fracture elongation of 40%)[20–22]. Meanwhile, the wear resistance of the Ti-25Nb-10Zr alloy has been demonstrated to be markedly superior to that of conventional alloys, and its corrosion potential has been measured as 155 mV in electrochemical corrosion tests[20]. Guan et al[23] reported that the NbTiZr coatings prepared by laser cladding exhibit superior wear resistance, with a wear rate only 17% of that of the commercially pure zirconium substrate. Furthermore, the elemental composition plays a critical role in determining the properties of RHEAs. Specifically, the synergistic interaction of the constituent elements promotes the formation of a stable solid solution, which in turn leads to a significant enhancement in performance. Studies have shown that alterations in elemental composition or content can modify the properties of the alloys[24–26]. In RHEA systems, grain refinement and the formation of Mo-containing passivation films are facilitated by the addition of Mo, and the wear resistance and corrosion resistance of RHEAs are significantly enhanced[27–30]. Lyu et al[31] revealed that the addition of Mo in $Al_{0.3}NbTiZrMo_x$ (x=0.1, 0.2, 0.3) reduced the corrosion rate in a 3.5wt% NaCl solution from 0.1637 mm/a to 0.0156 mm/a, while lowering the specific wear rate from 5.22×10^{-4} mm^3/(N · m) to 4.23×10^{-4} mm^3/(N · m). Using the laser cladding process, Du et al[32] prepared $TiZrHfNbTaMo_x$ (x=0, 0.25, 0.50, 0.75, 1) coatings with wear resistance notably superior to that of TC4 titanium alloy: the coefficient of friction (COF) was reduced by 35% under dry friction and by an additional 40% in a 3.5wt% NaCl solution.

The NbTiZr-based RHEAs exhibit significant potential for marine applications; however, their performance under aggressive abrasion-corrosion environments remains inadequate. To address this restriction, Mo was introduced as an alloying element for its proven capabilities in strengthening microhardness, refining microstructure, and improving passivation. This work systematically investigated the effects of Mo content on the microstructure, microhardness, wear resistance, and corrosion resistance of $NbTiZrMo_x$ alloys.

2 Experiment

The $NbTiZrMo_x$ RHEAs were prepared by vacuum arc melting using high-purity (99.99%) Nb, Ti, Zr, and Mo with an average particle size of 3 mm. Melting was conducted under an argon atmosphere at a current of 500 A in a water-cooled copper crucible. To ensure chemical homogeneity, each ingot was remelted at least ten times. The composition design of the $NbTiZrMo_x$ samples is shown in Table 1, namely Mo_0, $Mo_{0.1}$, $Mo_{0.3}$, $Mo_{0.5}$, $Mo_{0.7}$, and Mo_1.

The $NbTiZrMo_x$ RHEAs were cut into initial cubical samples of 10 mm×10 mm×3 mm using a wire cutter for microstructural analysis and property evaluation. Subsequently, the samples were ground to 2000# and polished to 0.02 μm using SiO_2 polishing compounds. The phase composition of the alloy was identified by a Smartlab-9KW X-ray diffractometer (XRD) with a voltage of 40 kV, a current of 30 mA, and a scan range from 20° to 80°. The microstructure of the alloy was characterized using a Leica DM4M optical microscope (OM) and a Phenom X scanning electron microscope (SEM).

The surface microhardness of the samples was measured by the Vickers hardness tester (FALCON 511) under a load of 500 g applied for 10 s. Wear tests were conducted at room temperature using an MRH-1 multi-functional friction and wear tester under a constant load of 200 N for 60 min, with a 2Cr13 stainless steel counter ring. Wear morphologies were examined using SEM and a KS52 non-contact surface profiler.

The corrosion resistance of the $NbTiZrMo_x$ alloys described in this work was characterized by a potentiostatic electrochemical test. Before the test, the oxide film on the surface of the sample was removed by grinding using SiC sandpaper. The sample was connected with copper wire and then sealed with epoxy resin. To reduce the error, care should be taken to ensure that the sample is fully immersed in the corrosion medium (3.5wt% NaCl aqueous solution). Additionally, electrochemical corrosion experiments were conducted using a CS350 electrochemical workstation, where the samples acted as the working electrodes, a saturated calomel electrode as the reference electrode, and a platinum mesh as the auxiliary electrode.

3 Results and Discussion

3.1 Phase constitution

XRD patterns (Fig. 1) confirm that $NbTiZrMo_x$ samples consist of a single bcc phase. This can be primarily attributed to the increased configurational entropy of mixing, which promotes the formation of simple, stable solid solution phases

Table 1 Composition design of $NbTiZrMo_x$ RHEAs (at%)

Sample	Nb	Ti	Zr	Mo
Mo_0	33.34%	33.33%	33.33%	0%
$Mo_{0.1}$	32.25%	32.25%	32.25%	3.25%
$Mo_{0.3}$	30.30%	30.30%	30.30%	9.10%
$Mo_{0.5}$	28.57%	28.57%	28.57%	14.29%
$Mo_{0.7}$	27.03%	27.03%	27.03%	18.91%
Mo_1	25.00%	25.00%	25.00%	25.00%

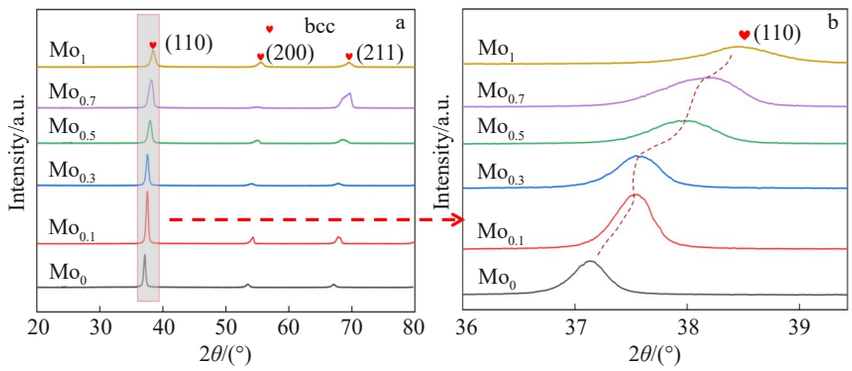

Fig.1 XRD patterns of $NbTiZrMo_x$ samples (a) and partial enlarged view (b)

in multi-principal-element alloys[33].

As shown in Fig. 1b, the (110) diffraction peak shifts towards higher angles with the increase in Mo content, indicating a gradual decrease in lattice parameter. Simultaneously, the combination of Eq. (1) and Eq. (2) yields lattice constants for the Mo_0, $Mo_{0.1}$, $Mo_{0.3}$, $Mo_{0.5}$, $Mo_{0.7}$, and Mo_1 samples of 0.3394, 0.3381, 0.3377, 0.3358, 0.3326, and 0.3311 nm, respectively. This variation is due to the small atomic radius of Mo (136 pm) compared to Nb (143 pm), Ti (142 pm), and Zr (160 pm). Specifically, as the Mo content increases, Mo atoms with smaller radii randomly occupy lattice sites in the bcc solid solution, causing the unit cell to contract. This contraction reduces interplanar spacing and ultimately induces lattice distortion. Simultaneously, the increase in Mo content also causes a slight broadening of the diffraction peaks, indicating that Mo addition promotes gradual grain refinement[34].

$$n\lambda = 2d\sin\theta \quad (1)$$

$$d = \frac{a}{\sqrt{h^2 + k^2 + l^2}} \quad (2)$$

where n denotes the diffraction order, d represents the interplanar spacing, 2θ is the diffraction angle, and λ stands for the wavelength of the incident X-ray. In Eq. (2), a refers to the lattice constant of the alloy, while h, k, and l are the Miller indices (i. e., crystal plane indices) corresponding to the diffracted crystal planes.

3.2 Microstructure

Fig. 2 shows SEM images of the $NbTiZrMo_x$ alloys, in which DR and ID denote the dendritic region and interdendritic region, respectively. The microstructure primarily consists of dendritic and interdendritic regions. In $NbTiZrMo_x$ alloys with higher Mo content, the dendritic structures become significantly finer. This result is consistent with the diffraction peak broadening observed in Fig.1b, which indicates grain refinement. This is because the nucleation rate of the alloy is enhanced by the addition of Mo, thereby suppressing the growth of coarse dendrites and resulting in dendrite refinement. More grain boundaries are generated by the grain refinement of the alloy, and dislocation motion is impeded by these boundaries, thus ultimately altering the properties of the alloy.

Two points, DR and ID, were selected from the corresponding microstructural regions shown in Fig. $2a_1$ – $2f_1$, and the corresponding EDS results of these two points are presented in Table 2. The results show that element segregation is observed between the dendritic and interdendritic regions of the alloys. For the Mo_0 alloy, elements Nb, Ti, and Zr are distributed relatively homogeneously. For the $Mo_{0.1}$, $Mo_{0.3}$, $Mo_{0.5}$, $Mo_{0.7}$, and Mo_1 alloys, Ti and Zr gather in the interdendritic region, and Nb and Mo are predominantly distributed in the dendritic region. This segregation of alloying elements is correlated with their solidification characteristics. This suggests that during the arc-melting preparation of the alloys, high-melting-point Nb and Mo are preferentially enriched in the solidifying dendrite arms due to the rapid cooling rates, whereas low-melting-point Ti and Zr are enriched in the interdendritic region.

3.3 Surface microhardness

Fig. 3 shows the average microhardness of $NbTiZrMo_x$ alloys with different Mo contents. The average microhardness of the Mo_0, $Mo_{0.1}$, $Mo_{0.3}$, $Mo_{0.5}$, $Mo_{0.7}$, and Mo_1 samples is 258, 288, 340, 387, 403, and 453 $HV_{0.5}$, respectively. It is evident that with the increase in Mo content, the average microhardness of the alloys gradually increases. Compared to the Mo_0 alloy, the Mo_1 alloy exhibits an approximately 70% increase in microhardness. This indicates that the addition of Mo is beneficial for improving the microhardness of $NbTiZrMo_x$ alloys. This can be attributed to the synergistic effects of grain refinement and solid solution strengthening induced by element Mo. During the rapid heating and cooling preparation process of RHEAs, changes in grain size take place, resulting in the formation of numerous fine grains and thereby generating a fine-grain strengthening effect[35,37]. Furthermore, the dissolution of Mo (characterized by a smaller atomic radius) into the bcc matrix phase induces considerable lattice distortion, which generates an effect that remarkably enhances the solid solution strengthening of the alloy[37].

3.4 Wear resistance

The friction and wear tests on $NbTiZrMo_x$ alloys were conducted at room temperature. Two-dimensional side profiles and macroscopic morphologies of $NbTiZrMo_x$ alloys after wear (Fig.4), as well as the wear width and wear depth of the alloys (Table 3), were used as indicators for evaluating the wear resistance of the alloys, and the wear rates (ω) of the

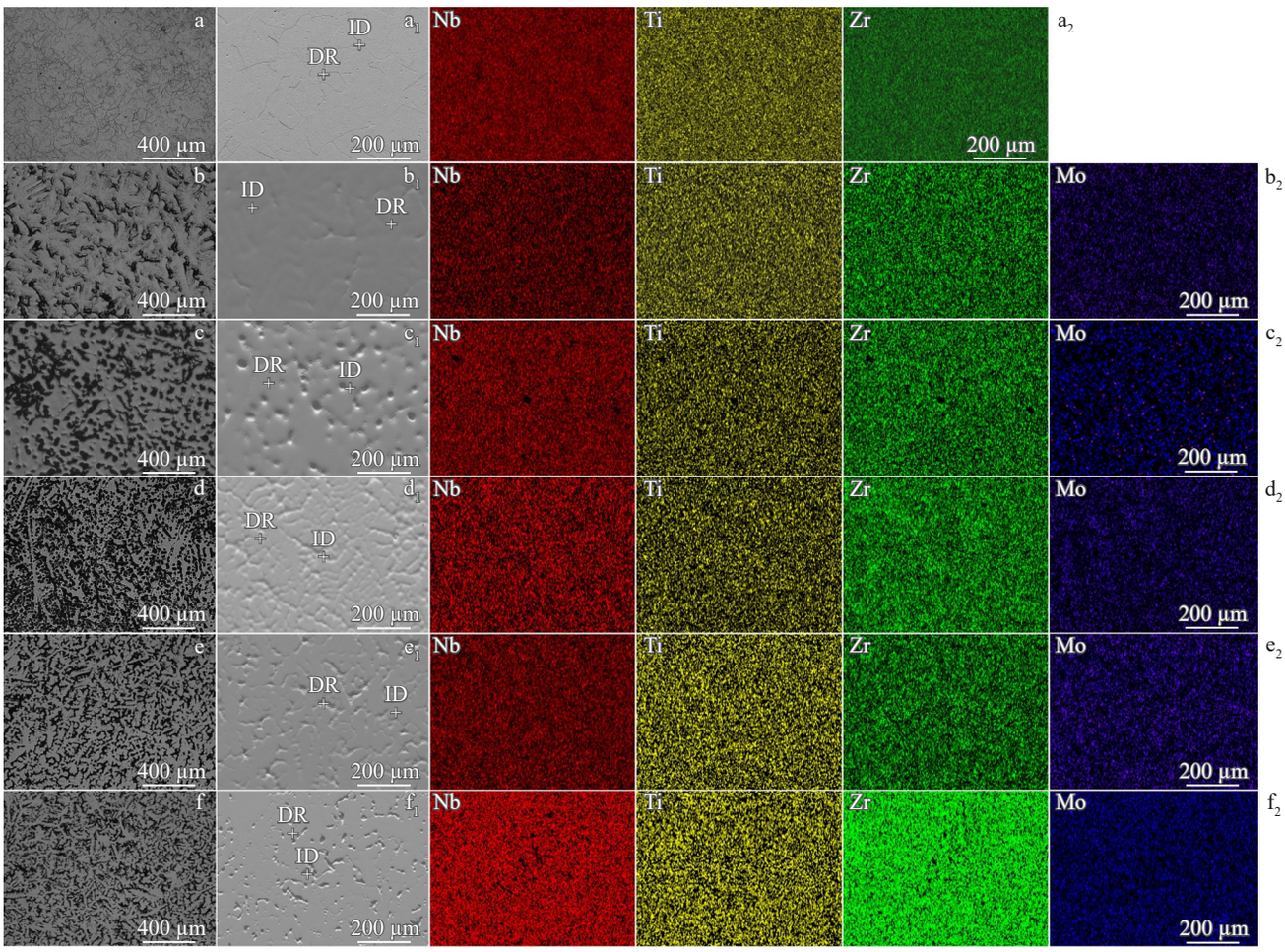

Fig.2 SEM microstructures (a–f, a_1–f_1) of $NbTiZrMo_x$ samples and corresponding EDS element mappings (a_2–f_2): (a–a_2) Mo_0; (b–b_2) $Mo_{0.1}$; (c–c_2) $Mo_{0.3}$; (d–d_2) $Mo_{0.5}$; (e–e_2) $Mo_{0.7}$; (f–f_2) Mo_1

Table 2 EDS results of different points marked in Fig.2a_1–2f_1 (at%)

Sample	Point	Nb	Ti	Zr	Mo
Mo_0	DR	34.27	32.65	33.08	0
	ID	34.7	32.71	32.59	0
$Mo_{0.1}$	DR	34.59	32.53	31.74	1.14
	ID	28.66	34.07	36.65	0.79
$Mo_{0.3}$	DR	32.38	29.88	29.22	8.52
	ID	28.75	36.64	29.53	5.08
$Mo_{0.5}$	DR	39.97	24.96	17.89	17.18
	ID	21.76	29.23	37.18	11.20
$Mo_{0.7}$	DR	30.78	25.16	22.63	21.43
	ID	22.05	26.30	33.56	18.09
Mo_1	DR	25.69	22.30	25.15	26.86
	ID	20.32	31.93	23.89	20.86

alloy samples was calculated using Eq. (3).

$$\omega = \frac{m}{L} \tag{3}$$

where m represents the mass loss (g), and L represents the wear length (m).

The cross-sectional profiles show that the Mo_0 alloy exhibits a deeper wear depth (75.73 μm), a wider wear width (10 406 μm), and a wear rate of (4.45×10^{-4} g/m). The wear depth, wear width, and wear rate gradually decrease as Mo content increases in $NbTiZrMo_x$ alloys. Furthermore, it can be seen that as the Mo content increases from 0.3 to 0.5, the wear depth decreases drastically, yielding a value significantly lower than that of the Mo_0 alloy. Based on the microstructure analysis, the addition of Mo in $NbTiZrMo_x$ refines dendrites and markedly increases grain boundary density. This dual effect (i.e., dendrite refinement and increased grain boundary

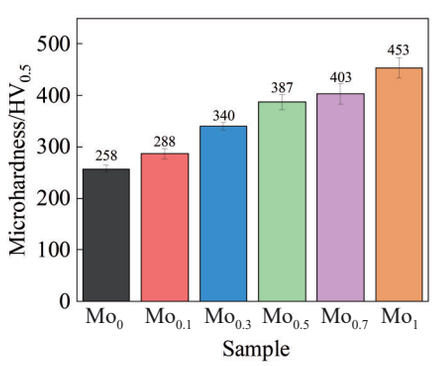

Fig.3 Microhardness of $NbTiZrMo_x$ samples

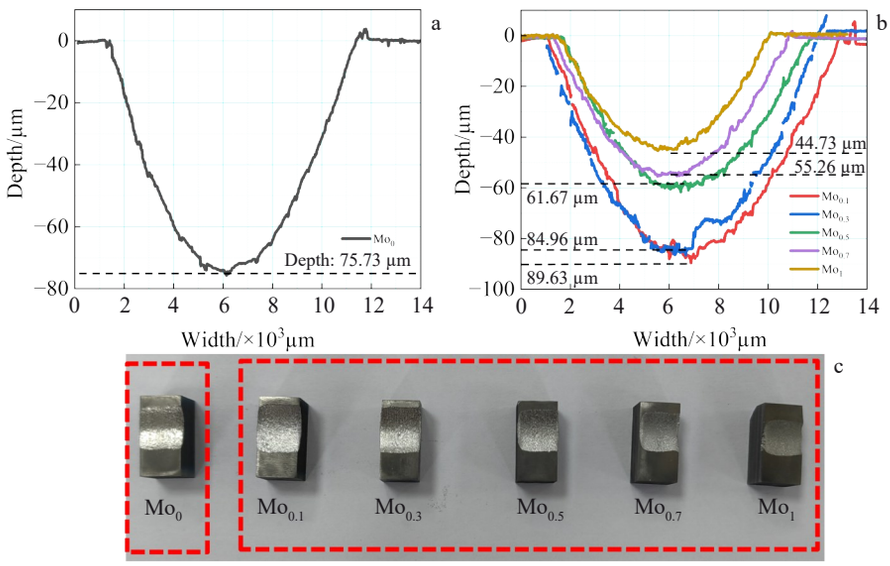

Fig.4 Two-dimensional cross-sectional profiles (a–b) and macroscopic morphologies (c) of different NbTiZrMo$_x$ samples after wear

Table 3 Wear width, wear depth, and wear rate of NbTiZrMo$_x$ samples

Sample	Wear width/ μm	Wear depth/ μm	Wear rate/ $\times10^{-4}$ g·m^{-1}
Mo_0	10 406	75.73	3.26
$Mo_{0.1}$	11 830	89.63	4.45
$Mo_{0.3}$	11 259	84.96	4.40
$Mo_{0.5}$	10 120	61.67	3.12
$Mo_{0.7}$	9 650	55.26	2.66
Mo_1	8 750	44.73	2.01

density) increases the microhardness of alloys through grain refinement strengthening, thereby alleviating wear severity. Meanwhile, the dense grain boundaries impede the initiation and propagation of cracks, minimizing material spalling[38].

Fig. 5 shows COF-distance curves for NbTiZrMo$_x$ RHEAs under a load of 200 N at room temperature. COF curves for all samples exhibit significant fluctuations during the early stages of wear, primarily due to unstable contact between the counter ring and the sample surface[39]. As time progresses, the fluctuations in COF of the samples significantly decrease and tend to stabilize. COF curves of the samples during the steady-state wear stage are similar and exhibit essentially consistent trends. As shown in Fig. 5, the average COFs of the Mo_0, $Mo_{0.1}$, $Mo_{0.3}$, $Mo_{0.5}$, $Mo_{0.7}$, and Mo_1 samples are 0.598, 0.654, 0.626, 0.558, 0.478, and 0.429, respectively. With increasing Mo content, the average COF of the alloys gradually decreases, which is consistent with the earlier trend in wear rate variation.

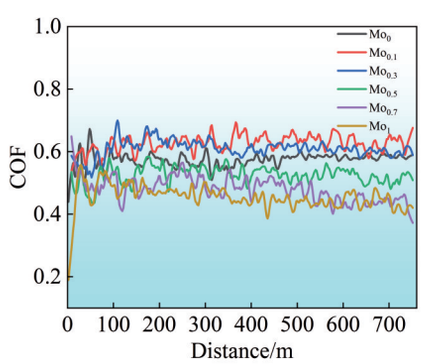

Fig.5 COF-distance curves of NbTiZrMo$_x$ RHEAs

To analyze the wear mechanisms of alloy samples with different Mo contents, SEM and EDS characterizations were performed on the worn surfaces of the samples, and the three-dimensional (3D) profiles of their wear interfaces were analyzed. As illustrated in Fig. 6, the surfaces of the Mo_0, $Mo_{0.1}$, and $Mo_{0.3}$ samples exhibit high susceptibility to wear under a friction load of 200 N and a duration of 60 min, which can be attributed to their relatively low microhardness values. Large debris particles are embedded into the mating ring under high loads, and extensive plow grooves on the sample surface are created by the plowing effect induced by reciprocating friction, leading to surface spalling of the alloys and delamination at the wear interfaces[40]. Additionally, due to the high oxygen affinity of Ti-containing alloys, high temperatures generated by the relative friction between the counter ring and sample surface during ambient dry sliding wear tests can readily induce the formation of an oxide layer. This layer accelerates further oxidative wear. If the layer is not removed promptly, it will break into abrasive particles and trigger abrasive wear. Oxidative wear is also exhibited by similar alloys like Ti-29Nb-14Ta-45Zr under dry sliding wear conditions[41]. Therefore, the oxygen distribution on the alloy surfaces was characterized by SEM-EDS. As shown in Fig. 6 and Table 4, all alloy surfaces exhibit relatively high oxygen content, with element O covering the sample surfaces, indicating the occurrence of oxidative wear. Wu et al[42] found that oxides on the alloy surface contribute to improved wear resistance. The surfaces of the Mo_0, $Mo_{0.1}$, and $Mo_{0.3}$ alloys are rich in oxygen. The coexistence of debris (marked by red

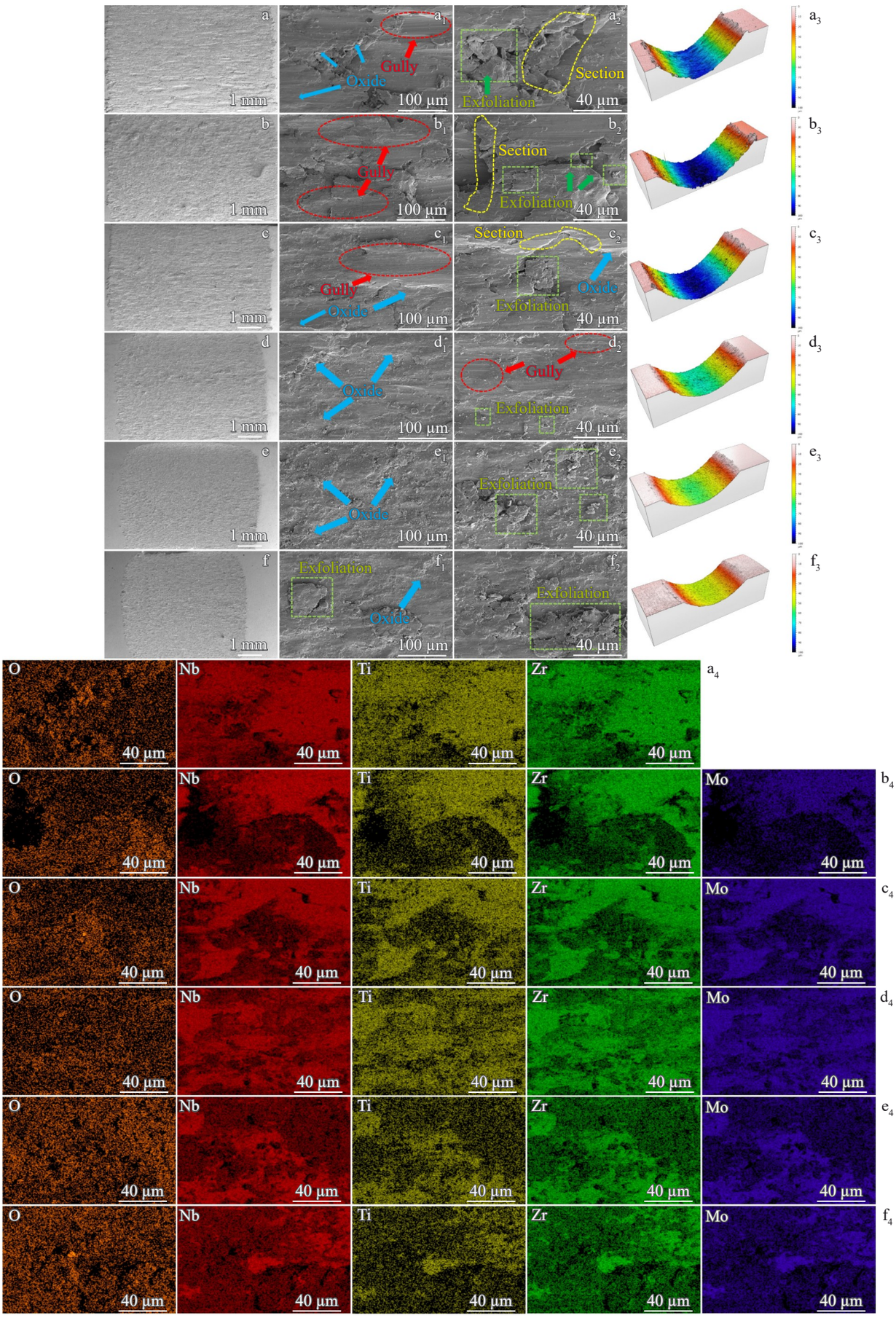

Fig.6 SEM images (a–f, a_1–f_1, a_2–f_2) and 3D morphologies (a_3–f_3) of $NbTiZrMo_x$ samples: (a–a_4) Mo_0; (b–b_4) $Mo_{0.1}$; (c–c_4) $Mo_{0.3}$; (d–d_4) $Mo_{0.5}$; (e–e_4) $Mo_{0.7}$; (f–f_4) Mo_1; EDS element mappings (a_4–f_4) corresponding to Fig.6a_2–6f_2

Table 4 Elemental content of worn surface (at%)

Sample	O	Nb	Ti	Zr	Mo
Mo_0	27.48	26.35	23.67	22.50	0
$Mo_{0.1}$	19.00	27.70	28.26	24.99	0.05
$Mo_{0.3}$	19.48	26.43	25.07	23.48	5.55
$Mo_{0.5}$	19.20	25.14	24.23	22.81	8.63
$Mo_{0.7}$	37.26	19.88	18.59	14.60	9.67
Mo_1	55.89	14.05	12.39	9.89	7.79

ellipses), extensive plow grooves, and certain oxidation products (marked by blue arrows), along with pronounced depth and width in their 3D profiles, is revealed by SEM images. Moreover, extrusion features (marked by green frames in Fig.6) are observed in local regions, suggesting that the wear mechanism is dominated by adhesive wear, coupled with the effects of abrasive wear and oxidative wear, ultimately resulting in relatively high wear rates and COF.

As the Mo content increases further, the O content on the worn surface is increased, the number of plow grooves is reduced, and the adhesivetear marks are less pronounced. The reduction in spalling particles indicates that the oxide film gradually produces an isolating effect, and oxidative wear dominates. Simultaneously, abrasive wear is induced by the detachment of metal flakes. 3D wear depth and width of the alloy are reduced; oxidative wear is the primary mechanism, with only minor abrasive wear occurring. COF and wear rate are reduced, and wear resistance is gradually enhanced. Lyu et al[43] have demonstrated that oxidative wear contributes to reducing the wear extent, which is consistent with the observed results.

In summary, as the Mo content increases in $NbTiZrMo_x$ alloys, the overall smoothness of the worn surface is gradually improved, adhesive and abrasive wear are progressively diminished, and oxidative wear emerges as the dominant wear mechanism, leading to the continuous improvement of wear performance.

3.5 Corrosion resistance

The Tafel polarization curves of $NbTiZrMo_x$ alloy in a 3.5wt% NaCl solution are shown in Fig. 7. The corrosion potential reflects the thermodynamic trend of corrosion, while the corrosion current density is attributed to the corrosion rate of the alloys. Moreover, all alloys exhibit distinct passivation in the 3.5wt% NaCl solution. The presence of a passivation region indicates that the alloy surface is undergoing passivation at this time, forming a protective film that impedes the corrosion process in the electrolyte solution. As the voltage increases to a certain level, there is a steep rise in current density, indicating either destruction of the passivation film on the material surface or pitting[44–45].

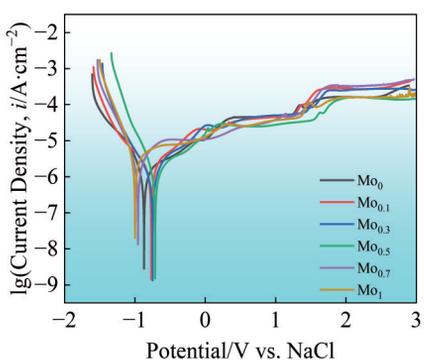

Fig.7 Tafel polarization curves of $NbTiZrMo_x$ alloys in 3.5wt% NaCl solution

As shown in Table 5, the addition of appropriate amounts of Mo can improve the corrosion resistance of $NbTiZrMo_x$, and $Mo_{0.5}$ has the lowest corrosion current density and corrosion rate. The I_{corr} of $Mo_{0.5}$ sample is measured to be 4.27×10^{-7} A/cm^2, which is remarkably lower than the I_{corr} values of as-cast $VZrTa_{0.5}Ti_x$ (x=0.25, 0.5, 0.75, 1, 1.25) alloys, which are 3.26×10^{-6}, 3.30×10^{-6}, 2.71×10^{-6}, 2.52×10^{-6}, and 2.59×10^{-6} A/cm^2, respectively[50].

Fig. 8 shows the electrochemical impedance spectroscopy (EIS) plots of the $NbTiZrMo_x$ RHEAs in a 3.5wt% NaCl solution, which reveal the relationship between impedance modulus and phase angle. As shown in Fig. 8a, the Nyquist plot reveals the capacitive reactance characteristic, showing the blocking effect between the electrolyte and the sample surface during electron transfer. Generally, a larger capacitive arc radius indicates a greater impedance of the sample and consequently a higher corrosion resistance. The Nyquist plots of the six alloys feature similarly shaped capacitive arcs. The arc radius initially expands with the increase in Mo content, reaches a maximum, and subsequently decreases. The $Mo_{0.5}$ alloy exhibits the largest capacitive arc radius, signifying the greater electrode reaction resistance, slower corrosion rate, and better corrosion resistance.

It is shown in Fig. 8b – 8c that a higher impedance of the alloys is correlated with a phase angle closer to 90°, indicating a more stable passivation film on the alloy surface, a lower corrosion rate, and superior corrosion resistance[46–48]. The $Mo_{0.5}$ alloy exhibits the largest semicircular arc diameter, the highest impedance, and the phase angle closest to 90° , indicating that the passivation film formed on its surface is the most stable among all the alloys.

The corrosion morphologies of the $NbTiZrMo_x$ alloys after potentiodynamic polarization testing in 3.5wt% NaCl solution are shown in Fig.9. Pitting corrosion is observed on all alloy surfaces. The Mo_0 alloy surface shows numerous deep black

Table 5 Electrochemical parameters of $NbTiZrMo_x$ RHEAs

Sample	E_{corr}/V	I_{corr}/×10^{-7} A·cm^{-2}
Mo_0	−0.874	7.520
$Mo_{0.1}$	−0.7883	7.220
$Mo_{0.3}$	−0.7847	5.030
$Mo_{0.5}$	−0.756	4.270
$Mo_{0.7}$	−0.926	7.828
Mo_1	−1.000	17.42

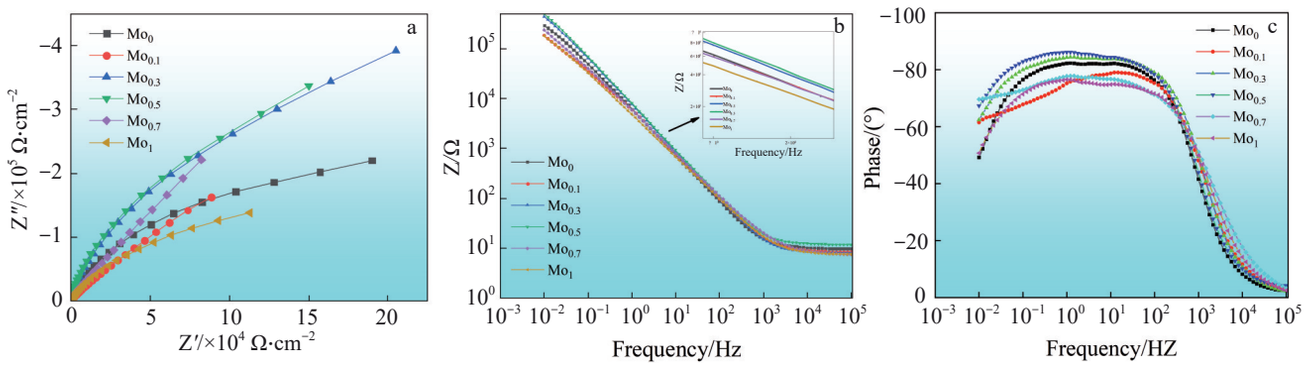

Fig.8 EIS plots of NbTiZrMo$_x$ RHEAs in 3.5wt% NaCl solution: (a) Nyquist plot; (b) Bode magnitude plot; (c) Bode phase plot

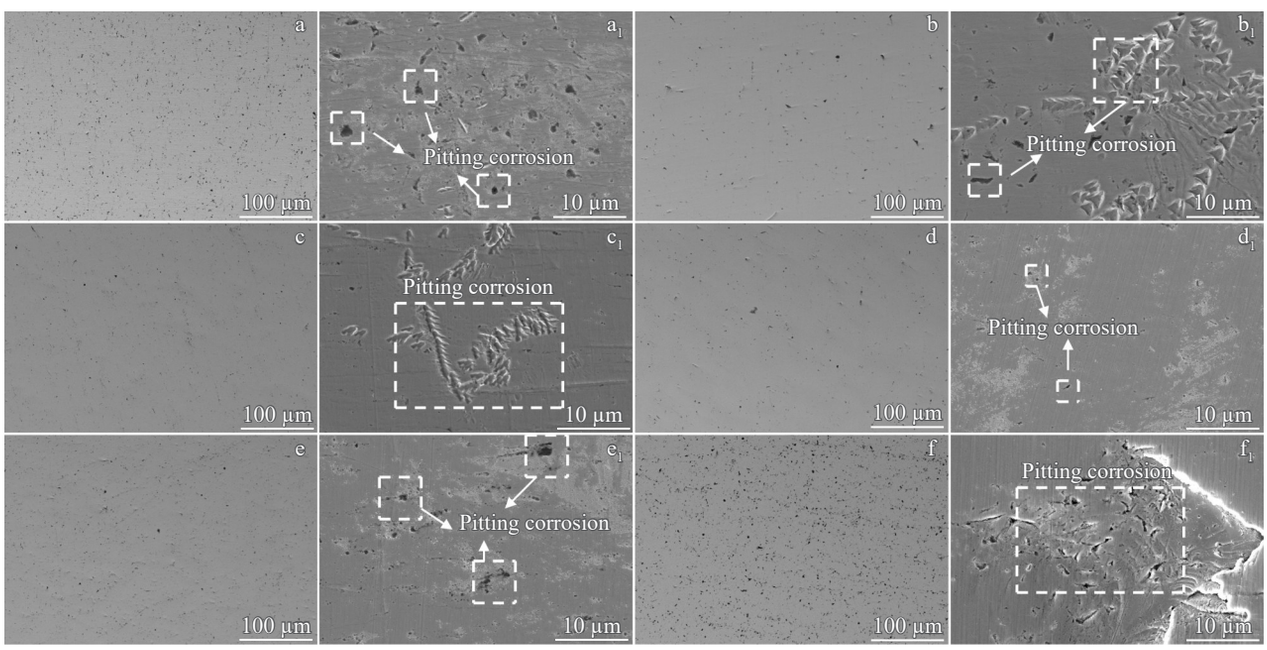

Fig.9 Corrosion morphologies of NbTiZrMo$_x$ RHEAs after electrochemical testing in 3.5wt% NaCl solution: (a – a$_1$) Mo$_0$; (b – b$_1$) Mo$_{0.1}$; (c–c$_1$) Mo$_{0.3}$; (d–d$_1$) Mo$_{0.5}$; (e–e$_1$) Mo$_{0.7}$; (f–f$_1$) Mo$_1$

pits. As Mo content increases, both black deep pits and gray shallow continuous pits are observed on Mo$_{0.1}$ and Mo$_{0.3}$ sample surfaces. The Mo$_{0.3}$ alloy surface displays abundant gray shallow pits. The number of pits decreases sharply on Mo$_{0.5}$ alloy surface. With further increases in Mo content, deeper and larger black pits predominate on Mo$_{0.7}$ and Mo$_1$ alloy surfaces, indicating more severe localized corrosion. For x≤0.5, the number of pits decreases with increasing Mo content, suggesting that an appropriate amount of Mo enhances corrosion resistance, particularly by inhibiting pitting initiation. However, for x>0.5 (e. g., x=0.7, 1), the number and size of pits increase significantly, indicating that excessive Mo increases pitting susceptibility and severely degrades local corrosion resistance.

The passive film formed on RHEA surface during the electrochemical test was characterized by XPS. Fig. 10 presents XPS results for the O 1s, Ti 2p, Zr 3d, Nb 3d, and Mo 3d spectra of NbTiZrMo$_x$ alloys. All binding energies have been adjusted for the charge effect of the C 1s line at 284.8 eV. The Ti 2p spectrum can be decomposed into two constituent peaks, the strong peak at 458.5 eV and the weak peak at 464.2 eV, which confirm the existence of Ti^{4+} (TiO_2) oxide state. Additionally, the Zr 3d and Nb 3d spectra show Zr^{4+} (182.7 and 185.1 eV) and Nb^{5+} (207.5 and 210.2 eV) peaks. This indicates that elements Nb and Zr in the alloy surface passivation film primarily exist as Nb_2O_5 and ZrO_2. Notably, Mo exhibits significant peak intensity differences at higher binding energies. The Mo 3d peak can be resolved into Mo^{6+} (232.7 and 235.8 eV), Mo^{4+} (234.5 and 231.4 eV), and metallic Mo (227.5 eV). Typically, the presence of Mo^{6+} in the passive film significantly suppresses pitting corrosion in Mo-containing alloys, contributing to enhanced corrosion resistance of RHEAs[28,49].

Furthermore, the excellent corrosion resistance of the Mo$_{0.5}$ alloy is mainly attributed to the valence state distribution characteristics of its Mo species: low-valent Mo species (e.g., Mo^{4+}) are present in a relatively high proportion, while high-valent Mo^{6+} is present in a relatively low proportion (Fig. 10). Specifically, MoO_2, the oxide corresponding to Mo^{4+}, exhibits poor stability and is prone to dissolution in corrosive media.

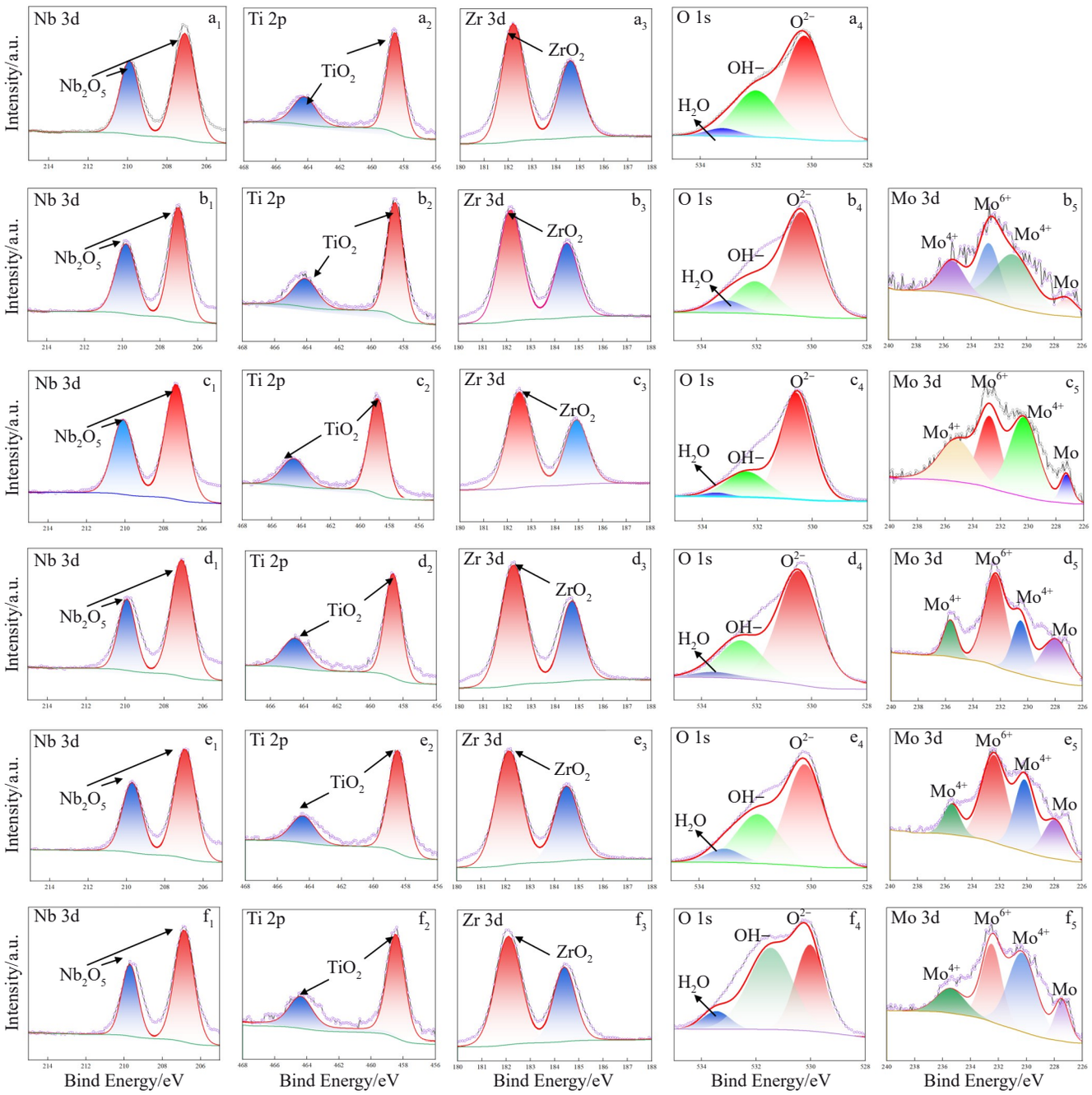

Fig.10 High-resolution XPS spectra of NbTiZrMo$_x$ RHEAs in 3.5wt% NaCl solution: (a_1–a_4) Mo_0; (b_1–b_5) $Mo_{0.1}$; (c_1–c_5) $Mo_{0.3}$; (d_1–d_5) $Mo_{0.5}$; (e_1–e_5) $Mo_{0.7}$; (f_1–f_5) Mo_1

In contrast, MoO_3, the oxide corresponding to Mo^{6+}, possesses higher stability and is crucial for maintaining the integrity and compactness of the passive film.

Fig. 11 illustrates the corrosion mechanisms of $Mo_{0.5}$ and $Mo_{0.7}$ samples in a 3.5wt% NaCl solution. Due to their different Mo contents, the two samples exhibit distinctly different corrosion evolution characteristics.

For the $Mo_{0.5}$ sample, the corrosion process begins with the migration of chloride ions (Cl^-) to the alloy surface and their interaction with the passive film and Mo-rich regions (Fig. 11a_1). Subsequently, Cl^- induces localized breakdown of the passive film, leading to substantial dissolution of metal ions. Among these dissolved ions, Mo is primarily oxidized to Mo^{6+}, resulting in the formation of initial corrosion pits (Fig.11a_2). Following this, partial repassivation takes place in some pitted regions. Metal ions, such as Nb^{5+}, Ti^{2+}, Zr^{2+}, and Mo^{6+}, react with oxygen ions (O^{2-}) to form a passive film composed of Nb_2O_5, ZrO_2, TiO_2, and MoO_3, which effectively suppresses further corrosion propagation, keeping the overall corrosion under control (Fig.11a_3).

In contrast, for the $Mo_{0.7}$ sample, the corrosion process also starts with the migration of Cl^- to the alloy surface and its interaction with the passive film (Fig. 11b_1). Initially, Cl^- causes localized damage to the passive film. Notably, due to the excessive Mo content and the restricted supply of oxygen ions (O^{2-}) in the environment, Mo cannot be fully oxidized to

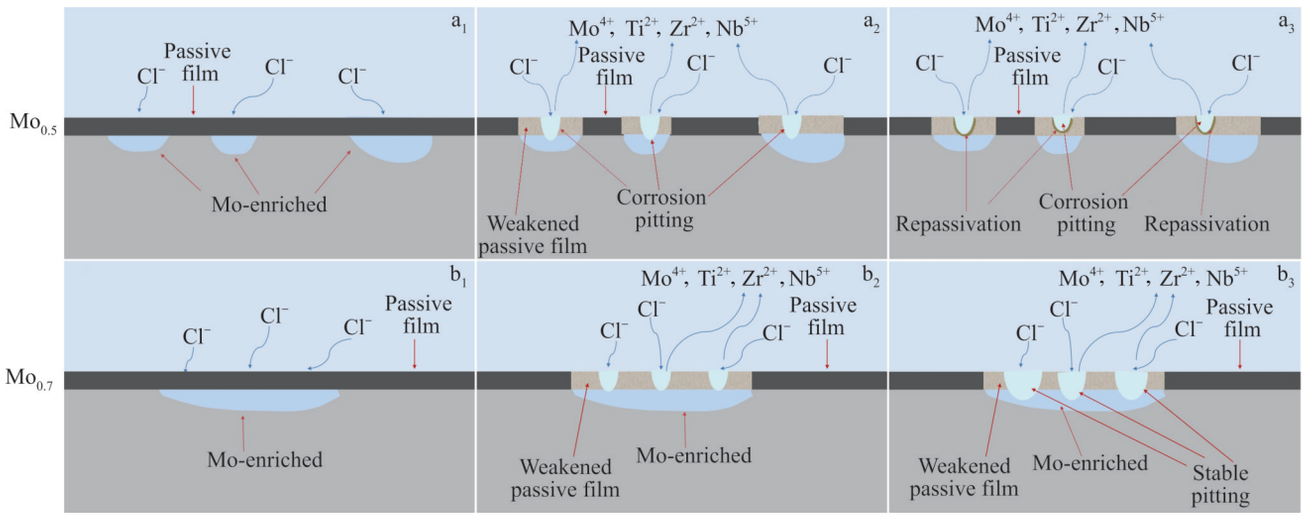

Fig.11 Schematic diagrams of corrosion mechanisms on surfaces of $Mo_{0.5}$ (a_1–a_3) and $Mo_{0.7}$ (b_1–b_3) samples in 3.5wt% NaCl solution

Mo^{6+}, leading to an increased proportion of Mo^{4+}. Consequently, a significant fraction of Mo exists mainly in the lower valence state of Mo^{4+} (Fig. $11b_2$). Metal ions, such as Nb^{5+}, Ti^{2+}, Zr^{2+}, and Mo^{4+}, react with oxygen ions (O^{2-}) to form a passive film composed of Nb_2O_5, ZrO_2, TiO_2, and MoO_2.

However, due to the relatively poor stability of MoO_2, it tends to dissolve in the 3.5wt% NaCl corrosive medium. This significantly impairs the repassivation capability in the pitted regions, allowing pitting to progress continuously and form larger pits. Ultimately, this leads to a sharp acceleration in corrosion rate and a substantial decline in corrosion resistance (Fig.$11b_3$).

Thus, the Mo content is a decisive factor governing passive film stability. An optimal Mo content (x=0.5) promotes film repair after initial breakdown, inhibiting further corrosion. Excessive Mo content disrupts the formation of a stable, protective film and accelerates the corrosion process.

4 Conclusions

1) The $NbTiZrMo_x$ alloys with a single bcc phase were prepared by vacuum arc melting. With the increase in Mo content, the grain size is reduced, while micro-segregation is intensified. Nb and Mo are enriched in dendritic regions, while Ti and Zr are accumulated in interdendritic regions.

2) The addition of element Mo effectively improves the microhardness and wear resistance of the alloy. This improvement can be attributed to the interplay of solid-solution strengthening and fine-grain strengthening caused by the presence of Mo. Furthermore, the wear mechanism transitions from dominant adhesive and abrasive wear to dominant oxidative wear with higher Mo content, which also contributes to the improved wear resistance.

3) The $NbTiZrMo_{0.5}$ alloy (Mo content of 14.29at%) exhibits the optimal corrosion resistance, characterized by minimal surface pitting. This is attributed to the formation of a dense composite passive film composed of MoO_3 synergistically combined with TiO_2, ZrO_2, and Nb_2O_5.

References

1 Li Y, Zhou Z L, He Y Y. *Materials*[J], 2023, 17(1): 65
2 Mirashi V U, Johnson S, Hegde S R *et al. Processing and Characterization of Materials: Select Proceedings of CPCM 2020*[M]. Singapore: Springer Singapore, 2021: 37
3 Liu Feiyang, Li Tianke, Wang Ruixin *et al. Rare Metal Materials and Engineering*[J], 2025, 54(3): 791 (in Chinese)
4 Yeh J W, Chen S K, Lin S J *et al. Advanced Engineering Materials*[J], 2004, 6(5): 299
5 Tsai M H, Yeh J W. *Materials Research Letters*[J], 2014, 2(3): 107
6 Zhang Y, Zhou Y J, Lin J P *et al. Advanced Engineering Materials*[J], 2008, 10(6): 534
7 Xiao B, Jia W P, Wang J *et al. Rare Metal Materials and Engineering*[J], 2023, 52(9): 3056
8 Wang M L, Lu Y P, Zhang G J *et al. Vacuum*[J], 2021, 184: 109905
9 Wei L, Qin W M, Chen J Y *et al. Corrosion Science*[J], 2023, 215: 111043
10 San S, Adhikari P, Sakidja R *et al. RSC Advances*[J], 2023, 13(51): 36468
11 Wang M L, Lu Y P, Lan J G *et al. Acta Materialia*[J], 2023, 248: 118806
12 Senkov O N, Wilks G B, Miracle D B *et al. Intermetallics*[J], 2010, 18(9): 1758
13 Huang X D, Qu R T, Ren F L *et al. Journal of Materials Research and Technology*[J], 2024, 31: 506
14 Jiang W T, Wang Y, Jiang B *et al. Rare Metal Materials and Engineering*[J], 2023, 52(3): 846
15 Zhou Y K, Zeng S, Zhu Y H *et al. Materials Letters*[J], 2022, 324: 132779
16 Hu Y L, Qu R T, Liu F. *Materials Today Communications*[J], 2025, 48: 113444
17 Hu S W, Li T J, Su Z *et al. Materials Science and Engineering B*[J], 2021, 270: 115226

18 Hu S W, Li T J, Li X *et al. Journal of Materials Science*[J], 2023, 58: 946
19 Senkov O N, Senkova S V, Woodward C *et al. Acta Materialia*[J], 2013, 61(5): 1545
20 Cotrut C M, Parau A C, Gherghilescu A I *et al. Metals*[J], 2017, 7(3): 86
21 Senkov O N, Scott J M, Senkova S V *et al. Journal of Alloys and Compounds*[J], 2011, 509(20): 6043
22 Guo C, Xing Y, Wu P *et al. Progress in Natural Science: Materials International*[J], 2024, 34(5): 1076
23 Guan H T, Chai L J, Wu J Y *et al. Intermetallics*[J], 2022, 143: 107498
24 Praveen S, Kim H S. *Advanced Engineering Materials*[J], 2018, 20(1): 1700645
25 Otto F, Yang Y, Bei H *et al. Acta Materialia*[J], 2013, 61(7): 2628
26 Miracle D B, Senkov O N. *Acta Materialia*[J], 2017, 122: 448
27 Wang H, Chen W P, Liu S Y *et al. Intermetallics*[J], 2024, 171: 108349
28 Wang K, Zhu Y, Wang P W *et al. Electrochimica Acta*[J], 2024, 480: 143951
29 Chen Zubin, Wang Xuhong, Tang Huaguo et al. *Rare Metal Materials and Engineering*[J], 2026, 55(1): 124 (in Chinese)
30 Poulia A, Georgatis E, Lekatou A *et al. Advanced Engineering Materials*[J], 2017, 19(2): 1600535
31 Lyu P, Guo S Y, Xia Z T *et al. Intermetallics*[J], 2024, 173: 108418
32 Du Z, Su Y, Li J *et al. Surface and Coatings Technology*[J], 2025, 513: 132454
33 Dai C D, Zhao T L, Du C W *et al. Journal of Materials Science & Technology*[J], 2020, 46: 64
34 Butler T M, Chaput K J, Dietrich J R *et al. Journal of Alloys and Compounds*[J], 2017, 729: 1004
35 Armstrong R W. *Philosophical Magazine*[J], 2016, 96(29): 3097
36 Shen X Y, Guo Z H, Liu F *et al. Journal of Alloys and Compounds*[J], 2024, 990: 174459
37 Cheng P, Zhao Y H, Xu X T *et al. Materials Science and Engineering A*[J], 2020, 772: 138681
38 Zhao Y S, Zhang J, Song F Y *et al. Progress in Natural Science: Materials International*[J], 2020, 30(3): 371
39 Yang K, Shi X L, Zheng D *et al. RSC Advances*[J], 2015, 5(95): 77885
40 Li B Y, Zou P, Wang A Q *et al. Surface and Coatings Technology*[J], 2025, 502: 131986
41 Haftlang F, Zarei-Hanzaki A, Abedi H R *et al. Metals and Materials International*[J], 2020, 26(4): 467
42 Wu T T, Li Y, Liu G *et al. Wear*[J], 2020, 452: 203281
43 Lyu P, Chen Y N, Liu Z J *et al. Materials Research Express*[J], 2019, 6(12): 126520
44 Qiu Y, Thomas S, Gibson M A *et al. Corrosion Science*[J], 2018, 133: 386
45 Liu S Y, Duan J Q, Zhang M Y *et al. Corrosion Science*[J], 2024, 228: 111835
46 Yue P P, Zhang M, Zhao T *et al. Industrial Crops and Products*[J], 2024, 214: 118523
47 Ji P F, Li B, Chen B H *et al. Corrosion Science*[J], 2020, 170: 108696
48 Roh B, Macdonald D D. *Russian Journal of Electrochemistry*[J], 2007, 43(2): 125
49 Li X F, Liu X Y, Lei N *et al. Materials Today Communications*[J], 2023, 35: 106020
50 Zhang P H, Li X M, Zhang A X *et al. Intermetallics*[J], 2026, 191: 109175

Mo含量对$NbTiZrMo_x$难熔高熵合金微观组织、耐磨性和腐蚀行为的影响

徐连波[1]，李鑫磊[1]，贵永亮[1]，宋春燕[1]，龙海洋[2]，韩尚达[1]，杨玉升[1]，吴启明[1]

(1. 华北理工大学 冶金与能源学院，河北 唐山 063210)

(2. 华北理工大学 机械工程学院，河北 唐山 063210)

摘　要：以高纯度的Nb、Ti、Zr、Mo颗粒为原料，采用真空电弧炉制备了不同Mo含量的$NbTiZrMo_x$难熔高熵合金。系统探讨了Mo元素在合金中的作用，以及不同Mo含量对合金的微观组织、显微硬度、耐腐蚀性和耐磨性的影响。结果表明，$NbTiZrMo_x$合金具有单一的体心立方相结构，呈枝晶形貌。Mo通过晶粒细化和固溶强化显著提高了合金的显微硬度与耐磨性。随着Mo含量的增加，合金的磨损机制由以黏着磨损为主导、磨粒磨损与氧化磨损共同作用逐渐转变为氧化磨损和轻微的黏着磨损。在3.5wt% NaCl溶液中的电化学腐蚀测试表明，$NbTiZrMo_x$合金的耐腐蚀性随Mo含量增加呈先增强后减弱的规律，其中Mo含量为14.29at%时，合金的耐腐蚀性最佳，表明适量添加Mo能够促进稳定钝化膜的形成，从而显著提高合金的耐腐蚀性能。

关键词：$NbTiZrMo_x$难熔高熵合金；显微组织；耐腐蚀性；耐磨性

作者简介：徐连波，男，1990年生，硕士，华北理工大学冶金与能源学院，河北 唐山 063210，E-mail：xu_lianbo@sina.com